Journal of The Electrochemical Society

OPEN ACCESS

Feasibility and Limitations of High-Voltage Lithium-Iron-Manganese Spinels

To cite this article: Anna Windmüller *et al* 2022 *J. Electrochem. Soc.* **169** 070518

Journal of The Electrochemical Society, 2022 **169** 070518

Feasibility and Limitations of High-Voltage Lithium-Iron-Manganese Spinels

Anna Windmüller,[1,z] Tatiana Renzi,[2,3,4] Hans Kungl,[1] Svitlana Taranenko,[1] Emmanuelle Suard,[4] François Fauth,[5] Mathieu Duttine,[2] Chih-Long Tsai,[1] Ruoheng Sun,[1] Yasin Emre Durmus,[1] Hermann Tempel,[1] Peter Jakes,[1] Christian Masquelier,[3,6] Rüdiger-A. Eichel,[1,7] Laurence Croguennec,[2,6] and Helmut Ehrenberg[8]

[1]*Institute of Energy and Climate Research (IEK-9), Forschungszentrum Jülich, 52425. Jülich, Germany*
[2]*Univ. Bordeaux, CNRS, Bordeaux INP, ICMCB UMR 5026, F-33600, Pessac, France*
[3]*Laboratoire de Réactivité et de Chimie des Solides, Université de Picardie Jules Verne, NRS-UMR 7314, F-80039 Amiens Cedex 1, France*
[4]*Institut Laue-Langevin, 71 avenue des Martyrs, 38042 Grenoble, France*
[5]*CELLS-ALBA synchrotron, 08290 Cerdanyola del Vallès, Barcelona, Spain*
[6]*RS2E, Réseau Français sur le Stockage Electrochimique de l'Energie, FR CNRS 3459, F-80039 Amiens Cedex 1, France*
[7]*Institut für Materialien und Prozesse für elektrochemische Energiespeicher– und wandler, RWTH Aachen University, D–52074 Aachen, Germany*
[8]*Institute for Applied Materials (IAM), Karlsruhe Institute of Technology (KIT), Eggenstein-Leopoldshafen D-76344, Germany*

Positive electrodes with high energy densities for Lithium-ion batteries (LIB) almost exclusively rely on toxic and costly transition metals. Iron based high voltage spinels can be feasible alternatives, but the phase stabilities and optimal chemistries for LIB applications are not fully understood yet. In this study, $LiFe_xMn_{2-x}O_4$ spinels with x = 0.2 to 0.9 were synthesized by solid-state reaction at 800 °C. High-resolution diffraction methods reveal gradual increasing partial spinel inversion as a function of x and early secondary phase formation. Mössbauer spectroscopy was used to identify the Fe valences, spin states and coordination. The unexpected increasing lattice parameters with Fe substitution for Mn was explained considering the anion-cation average bond lengths determined by Rietveld analysis and Mn^{3+} overstoichiometries revealed by cyclic voltammetry. Finally, galvanostatic cycling of Li-Fe-Mn-spinels shows that the capacity fading is correlated to increased cell polarization for higher upper charging cut-off voltage, Fe-content and C-rate. The electrolyte may also contribute significantly to the cycling limitations.
 [DOI: 10.1149/1945-7111/ac7ef8]

Manuscript submitted January 28, 2022; revised manuscript received July 1, 2022. Published July 15, 2022.

Supplementary material for this article is available online

Current approaches to enhance the volumetric and gravimetric energy density of positive electrodes for Li-ion batteries (LIB) follow two lines of development. One is to enhance the specific capacities of the used electrode materials and the other is to increase their working voltages.[1–5] In the materials class of Li-Mn spinels, higher voltages are achieved by substituting Mn with transition metals like Ni, Fe or Co. The redox potentials associated to these cations in spinels are around 5 V vs Li/Li^+.[3,6,7] Research has been mostly focused on $LiNi_{0.5}Mn_{1.5}O_4$, where a two-electron process involving the $Ni^{4+/2+}$ redox couple provides a cell voltage of 4.7 V vs Li/Li^+, making available a specific capacity of 148 mAh g^{-1} at high voltage.[2] Attractive alternatives to $LiNi_{0.5}Mn_{1.5}O_4$ are $LiFe_xMn_{2-x}O_4$ spinels, as Fe is non-toxic, more sustainable and low-cost than Ni. Furthermore, substituting Mn by Fe results in even higher voltages (~5.1 V vs Li/Li^+).[5,8–10] However, a high degree of substitution of Fe for Mn (ideally beyond x = 0.5) has to be achieved to profit from the high voltage, as the electrochemically active redox couple $Fe^{4+/3+}$ provides a one-electron process only.[8,9]

$LiFe_xMn_{2-x}O_4$ crystallizes in the *Fd*-3*m* space group, with Li occupying the tetrahedral site (8*a* Wyckoff position) and the transition metals (TM) occupying the octahedral site (16*d* Wyckoff position).[10,11] This so-called normal spinel is the preferred structure for most of the known high voltage spinels.[2] However, the ligand field of the high spin Fe^{3+} ion gives no energetic preference for octahedral or tetrahedral oxygen coordination,[12] thus Fe can partially occupy the tetrahedral 8*a* (Li) site, while Li partially occupies the octahedral 16*d* (TM) site, especially for compositions with x > 0.5 in $LiFe_xMn_{2-x}O_4$.[13–15] Exclusive occupancy of the tetrahedral site by Fe would yield the so-called inverse spinel. The onset of spinel inversion was identified at x = 0.57 and a gradual increase of Fe localization in the tetrahedral 8*a* site was reported with increasing of x in $LiFe_xMn_{2-x}O_4$.[13,16]

In the $LiFe_xMn_{2-x}O_4$ spinel with x ⩽ 0.5, a solid solution between $LiMn^{3+}Mn^{4+}O_4$ (x = 0) and $LiFe_{0.5}{}^{3+}Mn_{0.5}{}^{3+}Mn^{4+}O_4$ (x = 0.5) is established, with Mn being substituted by Fe on the octahedral 16*d* site.[13,16,17] With increasing Fe substitution for Mn, the lattice parameter is reported to increase linearly.[13,14,16–22] However, the increase in lattice parameter cannot be explained by the isovalent substitution of high spin Mn^{3+} by high spin Fe^{3+}, as they exhibit the same ionic radius for the octahedral coordination (0.645 Å).[23] Therefore, different hypothesis to explain the increase in lattice parameter are postulated: Talik et al. suggest Fe^{3+} substitution for Mn^{4+} or Mn^{3+} in the low spin state, as they exhibit smaller ionic radii.[20] Whereas, Tsuji et al. and Gracia et al. found a hint to the existence of a small fraction of Fe^{4+} via Mössbauer spectroscopy.[13,17] The existence of Fe^{4+} would explain the increase of lattice parameters due to the substitution of Fe^{4+} for Mn^{4+}.[13,17] However, this Mössbauer signal has been center of debates in literature and was also assigned to Fe^{3+} in a tetrahedral environment[16,19,22] or Fe^{3+} in an oxygen deficient octahedral environment.[21] Up to now, the reason for the increasing lattice parameters in $LiFe_xMn_{2-x}O_4$ high voltage spinels remains as an open question.

First reports on the high voltage performance of $LiFe_xMn_{2-x}O_4$ spinel date back to 1998 by Kawai et al.[9] They reported a total

[z]E-mail: a.windmueller@fz-juelich.de

specific capacity of 125 mAh g^{-1} encompassing a high voltage capacity (>4.5 V vs Li/Li^+) of more than 40 mAh g^{-1} after charging the battery to 5.3 V vs Li/Li^+. After 37 cycles, the total discharge capacity was reduced to less than 90 mAh g^{-1}. Several follow up studies focused on improving the specific capacity and cycling stability by optimizing the synthesis and processing conditions for $LiFe_{0.5}Mn_{1.5}O_4$,[8,16,24–30] as well as for the series of $LiFe_xMn_{2-x}O_4$ spinels.[7,10,14,16–21,27,31–33] Despite the broad variety of different synthesis and processing conditions, such as precursors, synthesis temperatures and atmospheres, number of synthesis steps and electrode fabrication, three reasons can be identified for the specific capacity fading and low cycling stabilities: (i) powder morphology and surface area,[8,29,34] (ii) amount of Fe in $LiFe_xMn_{2-x}O_4$,[17,21] and (iii) upper charging cut-off voltage.[25,29] All three parameters determine the exposure of the $LiFe_xMn_{2-x}O_4$ electrode material at the interface with the organic electrolyte at high voltage. It is generally agreed that the operation of high voltage positive electrode materials—well beyond the electrochemical stability window of the commonly used liquid electrolytes[8,35,36]—causes fast capacity fading due to electrolyte oxidation.[3,37] Recently, the tremendous effort in research and development for high voltage stable electrolytes[38,39] might bring forward compatible electrode-electrolyte combinations for realizing high voltage LIB in the near future.

In the present work, a series of $LiFe_xMn_{2-x}O_4$ spinels with x = 0.2 to 0.9 is analyzed aiming for the maximal utilization of the $Fe^{4+/3+}$ redox couple for LIB. As previous studies relied on laboratory diffractometers with Cu sources, especially for the compositions beyond x = 0.5,[13,14,16,24] we hope to improve the understanding of the phase stabilities, spinel inversion characteristics and Fe solubility limitations by high resolution synchrotron radiation powder diffraction (SRPD) in combination with neutron diffraction (NPD). The crystal chemistry of the thereby identified spinel samples with successful Fe incorporation, but low levels of spinel inversion (i.e. x < 0.6 with < 5% Fe occupancy on the tetrahedral site), is analyzed further by Mössbauer spectroscopy for the electronic configuration and local environment of Fe, while cyclic voltammetry (CV) is used to identify the redox active species. Finally, galvanostatic cycling at different C-rates allows for the understanding of the electrochemical performances and cycling stabilities. The results provide a baseline for further improvements of $LiFe_xMn_{2-x}O_4$ spinels.

Experimental

$LiFe_xMn_{2-x}O_4$, with x ranging from 0.2 to 0.9, were prepared by a solid state reaction process.[40] Stoichiometric amounts of Li_2CO_3 (Sigma-Aldrich, ⩾ 99%) including 2 mol.-% Li-excess, MnO_2 (Alfa-Aesar, 99.9%) and Fe_2O_3 (Sigma-Aldrich, 99%) were homogenized and ground in a planetary ball mill for 2 h in polymethylacrylate (PMA) containers using zirconia balls and isopropanol as milling liquid. The isopropanol was removed from the slurry in a rotational evaporator. The powder mixtures were calcined in closed alumina crucibles at 800 °C with 48 h dwell time in a muffle furnace under air. The heating rate was 5 °C min^{-1} with free cooling to ambient temperature by switching off the furnace.

Preparation of positive electrode sheets encompassed the mixing of a slurry, tape casting, drying, calendering and a final vacuum drying. The slurry contained 80%(w/w) $LiFe_xMn_{2-x}O_4$ active material, 10% (w/w) carbon Super P (Alfa-Aesar) and 10%(w/w) polyvinylidene fluoride (PVDF) (Alfa-Aesar) dissolved in N-methyl-2-pyrrolidone (NMP) (Alfa-Aesar). A planetary mixer (THINKY) was used for the mixing steps. The slurry was tape casted on aluminum foils (GoodFellow) with a wet state film thickness of 150 μm. After drying at 80 °C, the positive electrode sheets were calendered, punched into disks with 12 mm diameter and dried again under vacuum at 100 °C. The tap density of the as prepared positive electrode sheets is around 5 mg cm^{-2}.

The particle size and the morphology of the calcined powders were investigated with a scanning electron microscope (SEM) (Quanta FEG 650 FEI, USA). The images were recorded operating the SEM at an accelerating voltage of 20.0 kV at magnifications of 10000 x with a secondary electron detector (ETD).

SRPD data were collected from fine-grained samples sealed in 0.7 mm diameter glass capillaries using the MSPD diffractometer at ALBA Synchrotron (Barcelona, Spain),[41] in Debye–Scherrer geometry, at 0.82411 Å in the 2θ angular range of 0.5°−72° with 0.006° 2θ-steps and an accumulation time of 5 min per pattern for the samples x = 0.2, 0.3, 0.5. For the samples with x = 0.4 and x = 0.6 to 0.9, the SRPD data were collected at 0.9532 Å in the 2θ angular range of 3.5°−62° applying the same step size and accumulation time. Complementary, NPD measurements were performed on the high-resolution powder diffractometer D2B at the Institut Laue Langevin (ILL, Grenoble, France).[42] The powders were placed in 8 mm diameter vanadium sample holders each. The diffraction patterns were collected at room temperature, with a wavelength of 1.5947(1) Å in the 2θ angular range of 0°−150° with 0.05° 2θ-steps during a total accumulation time of 6 h per pattern. For cross comparison, the results obtained from NPD and SRPD at different wavelengths will be expressed independent from the wavelength (λ) in Q-space as $Q = 4\cdot\pi\cdot\sin(\theta)/\lambda$. Rietveld analysis[43] of NPD and SRPD data was carried out using the GSAS II software package.[44]

^{57}Fe Mössbauer spectroscopy measurements were performed for x = 0.2 to 0.5 at room temperature using a constant acceleration Halder-type spectrometer operating in transmission geometry with a room temperature ^{57}Co source (embedded in a Rh matrix). The velocity scale was calibrated using a pure α-Fe^0 foil as reference material. The polycrystalline absorbers were prepared in order to contain less than 5 mg cm^{-2} of Fe and thus, avoid saturation effects. The Mössbauer hyperfine parameters (δ isomer shift, Δ quadrupole splitting, 2ε quadrupole shift, B_{hf} hyperfine magnetic field, Γ signal linewidth and relative areas) were refined using both homemade programs and the WinNormos® software (*Wissenschaftliche Elektronik GmbH*).

Electrochemical experiments on $LiFe_xMn_{2-x}O_4$ tapes with x = 0.2 to 0.5 were performed in Swagelok-type cells that were assembled in a glove box (MBraun Ecolab) under argon atmosphere. Li-foil (Alfa-Aesar), glass microfiber filter (Whatman) and 1 M $LiPF_6$ in 1:1 v/v ethylene carbonate / dimethyl carbonate (EC/DMC) (LP30, BASF) were used as negative electrode, separator and electrolyte, respectively. Electrochemical measurements were carried out by a VMP3 potentiostat system (BioLogic) by operating the cells in a climate chamber (Binder) at 23 °C. The CVs were recorded at a scan rate of 0.028 mV s^{-1} from 3.0 to 5.2 V vs Li/Li^+. Galvanostatic cycling was performed in the same voltage range at C/20 rates over 50 cycles. $LiFe_{0.5}Mn_{1.5}O_4$ was further investigated by galvanostatic cycling at different C-rates with intermediate cycling at a lower current density: i) At a C/10 rate for 50 cycles with two cycles at C/20 at the beginning and at the end of the cycling; ii) at C/5 for 2 series of 50 cycles with two intermediate cycles at C/20; and (iii) at 1 C for 10 series of 50 cycles with two intermediate cycles at C/20. The total cycling time of (i)–(iii) is approximately 900 h.

Results and Discussion

After calcination at 800 °C, $LiFe_xMn_{2-x}O_4$ powders consist of primary particles being 0.5–2 μm in size. Partially, these particles aggregate or form up to 10 μm sized sintered agglomerates. The SEM images of $LiFe_xMn_{2-x}O_4$ with x = 0.2, 0.4 and 0.7 are shown in Fig. 1. No substantial differences in particle size or morphology could be seen for the materials as a function of the Fe content.

Figure 2 displays the SRPD patterns of the $LiFe_xMn_{2-x}O_4$ samples for x = 0.2 to x = 0.9. Materials with spinel as single phase are obtained with a low Fe content (x < 0.4). For x = 0.4, 0.5 and 0.6 secondary phase reflections rise from the background with small intensities (closer inspection is offered in Fig. S1 (available online at stacks.iop.org/JES/169/070518/mmedia)). They can be indexed to a Li_2MnO_3 layered oxide that crystallizes in the

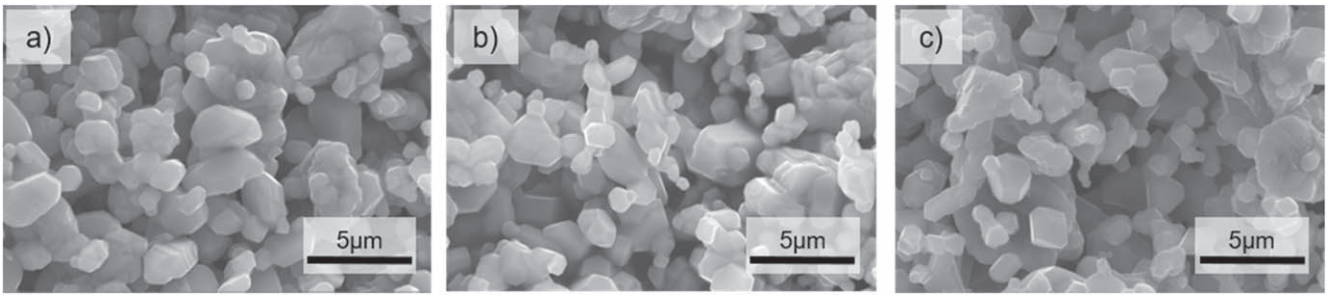

Figure 1. SEM of Lithium-Iron-Manganese spinel $LiFe_xMn_{2-x}O_4$, (a) x = 0.2, b) x = 0.4 and (c) x = 0.7.

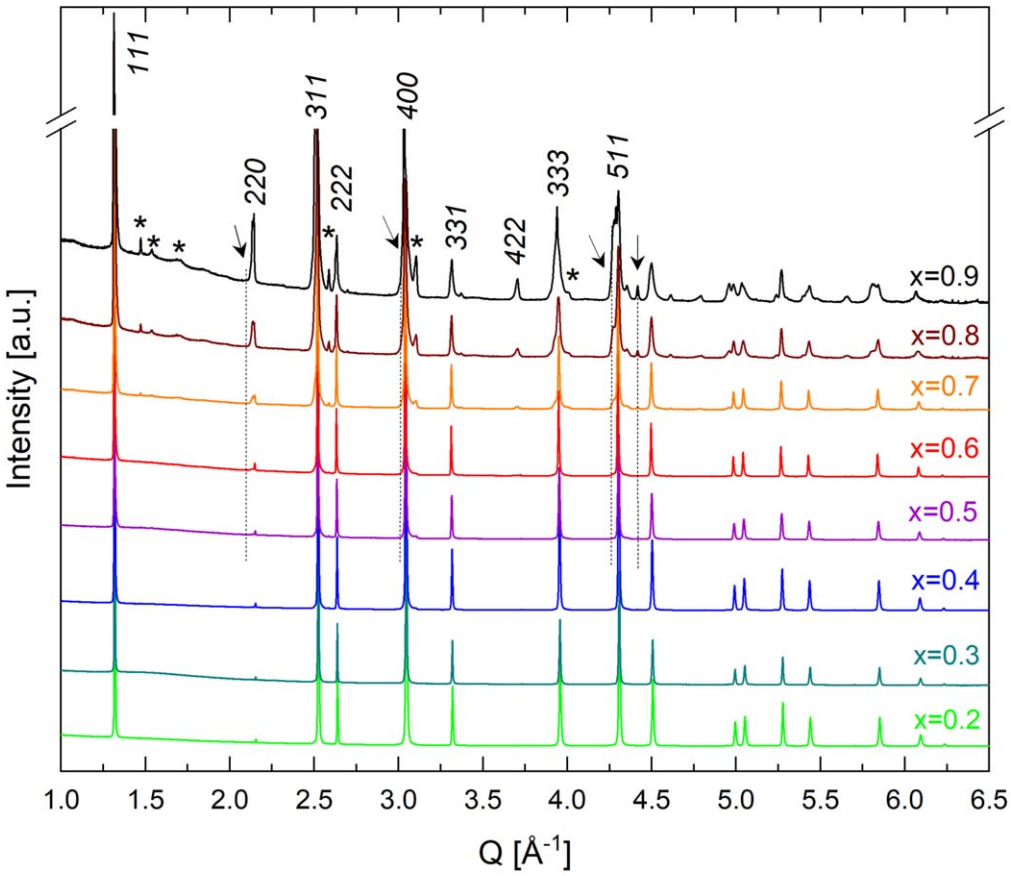

Figure 2. Synchrotron powder diffraction patterns for $LiFe_xMn_{2-x}O_4$ ($0.2 \leqslant x \leqslant 0.9$). Spinel reflections are indicated by their *hkl* Miller indices. Secondary phase reflections are highlighted with the symbol * for Li_2MnO_3 and arrows pointing to positions of $LiFe_5O_8$ reflections. Vertical dashed lines are drawn to guide the eye.

monoclinic C2/m space group with the cell parameters a = 4.9292 (2) Å, b = 8.5315(2) Å, c = 5.0251(1) Å, and β = 109.337(2)°.[45,46] Li_2MnO_3 is a well-known secondary phase in the Li-Mn-O system.[47] Since it is structurally related to spinel, many of its main reflections are superimposed by the reflections of the main spinel phase. The intensity of Li_2MnO_3 reflections increases significantly for $x \geqslant 0.7$. For those compositions, it can be easily identified in Fig. 2 from its typical *020*, *110* and *11−1* reflections (marked by * in the Q range from 1.5 to 2 $Å^{-1}$) with their well-known heterogeneous peak profile broadening due to stacking faults.[48] Additionally, shoulders emerge at the high-angle sides of the spinel reflections that also can be attributed to Li_2MnO_3.

Besides the obvious presence of Li_2MnO_3, shoulders at the low angle side of some spinel reflections, especially at the *220*, *311*, *400* and *511* reflections are visible for $x \geqslant 0.5$. Additionally, freestanding reflections at Q = 3.75 $Å^{-1}$ and Q = 4.4 $Å^{-1}$ emerge for these compositions. The positions of these shoulders and freestanding reflections can be attributed to a $LiFe_5O_8$ spinel with a = 8.33 Å.[49] The intensities of the additional reflections increase with the Fe content in the samples. This phase has not been identified in the $LiFe_xMn_{2-x}O_4$ system before. In previous studies, however, powder diffraction was exclusively carried out on laboratory diffractometers with Cu sources.[13,14,16,24] The lower signal to noise ratio and the lower instrumental resolution might have hidden any $LiFe_5O_8$ contribution or at least make its identification rather difficult.[16] The appearance of $LiFe_5O_8$ in the current study and its increase beyond x > 0.4 suggests that the solubility limit of Fe in $LiFe_xMn_{2-x}O_4$ under the given synthesis conditions is reached in between x = 0.4 to 0.5.

The structural parameters of the main spinel phase in the samples were further investigated by Rietveld analysis based on the synchrotron und neutron diffraction data. The SRPD data are collected with high resolution, and thus give high accuracy for the cell parameters and atomic positions, whereas the NPD data allow

the localization of the light element Li and the discrimination between the Mn and Fe due to the different sign of their coherent scattering lengths (−3.73 pm for Mn and 9.45 pm for Fe). Thus, structural parameters, such as lattice parameters and atomic positions, which allow for the determination of average bond distances, as well as cation occupancies and cation mixing on tetrahedral and octahedral sites, can be evaluated.

The refinement of the structural parameters starts from a *Fd-3m* model structure as $[Li,TM]^{8a}[Fe,Mn]^{16d}{}_2O^{32e}{}_4$, considering cation mixing of Li and TM on the tetrahedral *8a* site and cation mixing of Fe and Mn on the octahedral 16*d* site. Cation mixing of Li and TMs on the 16*d* site was not found to improve the fitting quality and was excluded from the model early. The structural parameters, such as lattice parameters, atomic displacement parameters, atomic positions (x = y = z position of oxygen), and site occupancies on tetrahedral and octahedral sites were refined first by SRPD. Cation mixing of Li and TM was allowed on tetrahedral sites and octahedral sites, by constraining the occupancy to 100%. Peak broadening through size and strain effects were treated individually. Finally, all parameters were freed to converge. The refined structural parameters from SRPD were used as starting values for the combined fit of the SRPD and NPD data. Site occupancies of Fe and Mn on the octahedral site, as well as Fe or Mn and Li on the tetrahedral site were constrained to 100% at each site and refined against the SRPD and NPD data in the combined approach. Additionally, the phases $LiFe_5O_8$ and Li_2MnO_3 were considered. This applied three phase model leads to a reasonable difference minimization of observed and calculated data for the samples $x \leqslant 0.5$ (Table I, Table S1).

For x = 0.6, the data could no more be reasonably described by the aforementioned three phase model. The calculated pattern leaves unfitted intensity residuals due to asymmetric peak shapes for the measured data that could not be calculated by the applied model. Figures S2 and S3 allow closer inspections of measured and calculated data and their difference plot for the x = 0.6 sample. The most reasonable explanation for the misfit is a large inhomogeneity of the main spinel phase, that might arise from accelerated Li_2MnO_3 and $LiFe_5O_8$ segregation, which points out the really low thermodynamic stability of the spinel, for the given synthesis temperature and atmosphere.

Table I gives a summary of the refined parameters for the $LiFe_xMn_{2-x}O_4$ samples with x = 0.2 to x = 0.5 and Figs. 3a and 3b display the measured and calculated data of SRPD and NDP and their difference plot exemplarily for x = 0.3. The refined lattice parameters *a* increase slightly from *a* = 8.2476 Å ± 0.00003 Å for x = 0.2 to *a* = 8.2582 Å ± 0.00003 Å for x = 0.5, which is an increase of 0.13%, in good agreement with the observed increase in lattice parameters for $LiFe_xMn_{2-x}O_4$ with $x \leqslant 0.5$ in literature.[16,18–21] Equally to the debate in literature, we have no direct explanation for the observation of increasing lattice parameters, as for the isovalent substitution of high spin Fe^{3+} (0.645 Å) for high spin Mn^{3+} (0.645 Å) in $LiFe^{3+}{}_xMn^{3+}{}_{1-x}Mn^{4+}O_4$ an increase in lattice parameter is not expected. We will discuss the problem again later after the evaluation of more obtained results.

The refinement of TM occupancies on the octahedral 16*d* site agrees to the expected cation mixing of Fe and Mn (Table I). That is, for $LiFe_{0.2}Mn_{1.8}O_4$ a Fe fraction of 9.8% ± 0.1% is found on the 16*d* site (vs 10% expected). Similarly, 14.9% ± 0.1% (vs 15% expected), 19.5% ± 0.1% (vs 20% expected) and 24.2% ± 0.1% (vs 25% expected) are found for $LiFe_xMn_{2-x}O_4$ with x = 0.3, 0.4 and 0.5, respectively. Furthermore, cation mixing of Li and Fe on the tetrahedral 8*a* sites was found to improve the fit for all compositions. The refined fractions of Fe on the tetrahedral site are 1.5% ± 0.2% for $LiFe_{0.2}Mn_{1.8}O_4$, 1.8% ± 0.2% for $LiFe_{0.3}Mn_{1.7}O_4$, 3.2% ± 0.2% for $LiFe_{0.4}Mn_{1.6}O_4$, and 4.0% ± 0.2% for $LiFe_{0.5}Mn_{1.5}O_4$. Accordingly, the resulting structural formulas can be written as $[Li_{0.98}Fe_{0.02}]^{8a}[Fe_{0.2}Mn_{1.8}]^{16d}O^{32e}{}_4$ for x = 0.2, $[Li_{0.98}Fe_{0.02}]^{8a}[Fe_{0.3}Mn_{1.7}]^{16d}O^{32e}{}_4$ for x = 0.3, $[Li_{0.97}Fe_{0.03}]^{8a}[Fe_{0.4}Mn_{1.6}]^{16d}O^{32e}{}_4$ for x = 0.4, and $[Li_{0.96}Fe_{0.04}]^{8a}[Fe_{0.49}Mn_{1.51}]^{16d}O^{32e}{}_4$ for x = 0.5, respectively.

While the increase of Fe occupation on the octahedral site is expected, the steady increase of Fe occupation on the tetrahedral *8a* site for $x < 0.5$ with increasing x is surprising. It suggests that spinel inversion starts much earlier than reported by Ohzuku et al. who defined the onset of spinel inversion sharply at x = 0.57 from the evaluation of the intensity ratios of the *220* and *400* spinel reflections.[16] It is in line with the SRPD and NPD studies of Shigemura et al. who found ∼ 3% of Fe occupying the *8a* site for x = 0.5.[19] These results point out the difficulties in targeting normal spinel type $LiFe_xMn_{2-x}O_4$ materials, given the nature of the ligand field of the Fe^{3+} ion, with equal stabilization energies for the tetrahedral and the octahedral coordination.[12]

Aliovalent substitution of Li^+ by Fe^{3+} on tetrahedral sites should affect the distance in between the cationic 8*a* and anionic 32*e* atomic site positions. Inspections of the bond lengths determined from the Rietveld refinement (Table I) show that the 8*a*–32*e* atomic distance decreases slightly from 1.967 ± 0.0005 Å for x = 0.2 to 1.965 ± 0.0005 Å for x = 0.5, in correlation to the rising Fe occupancy on the 8*a* site. Surprisingly, not only the 8*a*–32*e* atomic distance shows changes with x, but also the 16*d*–32*e* atomic distance. Cationic sites (8*a* at 1/8, 1/8, 1/8 and 16*d* at 1/2, 1/2, 1/2) are special positions with no free variables. Thus, the atomic distances of cations and anions in spinels are determined by the unit cell dimensions and the fractional coordinates of the oxygen position (32*e* at x, x, x), only. The changes in the oxygen position will determine the relative sizes of the octahedra and the tetrahedra in the unit cell. Consequently, a changing size of the tetrahedral cation-anion bond length will affect the size of the octahedral cation-anion bond length.[11] However, the observed increase in the 16*d*–32*e* atomic distance is far larger than the decrease in the 8*a*–32*e* atomic distance. While the 8*a*–32*e* atomic distance changes by 0.1% only, the 16*d*–32*e* atomic distance changes from 1.9629 ± 0.00004 Å for x = 0.2 to 1.9679 ± 0.00004 Å for x = 0.5, which is a change of 0.25%. Therefore, the changes in the octahedral cation-anion bond length cannot be explained by the counter-balancing effect from the decreased tetrahedral cation-anion bond length alone. Similar to the unexpected lattice parameter increase, the absolute increase of the 16*d*–32*e* atomic distance is unexpected from the cation mixing of Fe^{3+} and Mn^{3+} on the 16*d* site because of their identical radius.

One hypothesis to explain the increase in octahedral bond length would be through overstoichiometric fractions of high spin Mn^{3+} ions (0.645 Å) at the expense of the smaller Mn^{4+} ions (0.53 Å) on the octahedral site. Overstoichiometry in Mn^{3+} might result from the reduction of Mn^{4+} through oxygen loss during synthesis and formation of an oxygen-deficient spinel, a process that is well known in the Li-Mn-spinel system.[50,51] The presence of oxygen vacancies could not be directly verified from the Rietveld analysis, since the oxygen site's occupancy is highly correlated to the other structural parameters. However, it is worth mentioning that when freed to converge after fixing all refined parameters, the oxygen occupancy converges away from full occupancies to values around 97% to 98%, which might indicate the presence of oxygen defects. Thus, an overstoichiometric fraction of Mn^{3+} on the octahedral 16*d* site could explain an increasing average octahedral bond length with x, if in parallel the oxygen deficiency also increases with x – suggesting a destabilization of the anionic lattice of $LiFe_xMn_{2-x}O_4$ spinel because of Fe incorporation. This would agree with the increase of Li_2MnO_3 fraction with increasing x. Li_2MnO_3 is known for coexisting with an oxygen deficient spinel, hence its presence indicates oxygen deficiency and lower stability of the spinel.[50] Another hypothesis proposed in literature to explain this unexpected increasing lattice parameter is the presence of the unusual Fe^{4+} or a mixed $Fe^{3.5+}$ valence state.[13,17] These different hypotheses will be discussed in the following, especially by considering the Mössbauer spectroscopy results.

The electronic configuration and local environment of Fe in $LiFe_xMn_{2-x}O_4$ ($0.2 \leqslant x \leqslant 0.5$) were probed experimentally by ^{57}Fe Mössbauer spectroscopy in order to get more insight into the Fe

Table I. Refined structural parameters obtained for the $LiFe_xMn_{2-x}O_4$ samples with x = 0.2 to 0.5 by Rietveld analysis of SRPD and NPD data. *) wR: Weighted pattern residual.

x in $LiFe_xMn_{2-x}O_4$	Lattice parameter [Å]	Oxygen atomic position	8*a* Fe occupancy [%]	16*d* Fe occupancy [%]	8*a*–32*e* atomic distance [Å]	16*d*–32*e* atomic distance [Å]	wR*
0.2	8.24764(3)	0.26268(9)	1.5(2)	9.8(1)	1.9667(5)	1.96294(4)	7.5
0.3	8.24988(3)	0.26258(10)	1.8(2)	14.9(1)	1.9659(5)	1.96420(4)	8.2
0.4	8.25248(3)	0.26248(10)	3.2(2)	19.5(1)	1.9651(5)	1.96546(4)	8.7
0.5	8.25816(3)	0.26235(9)	4.0(1)	24.2(1)	1.9646(4)	1.96785(4)	8.1

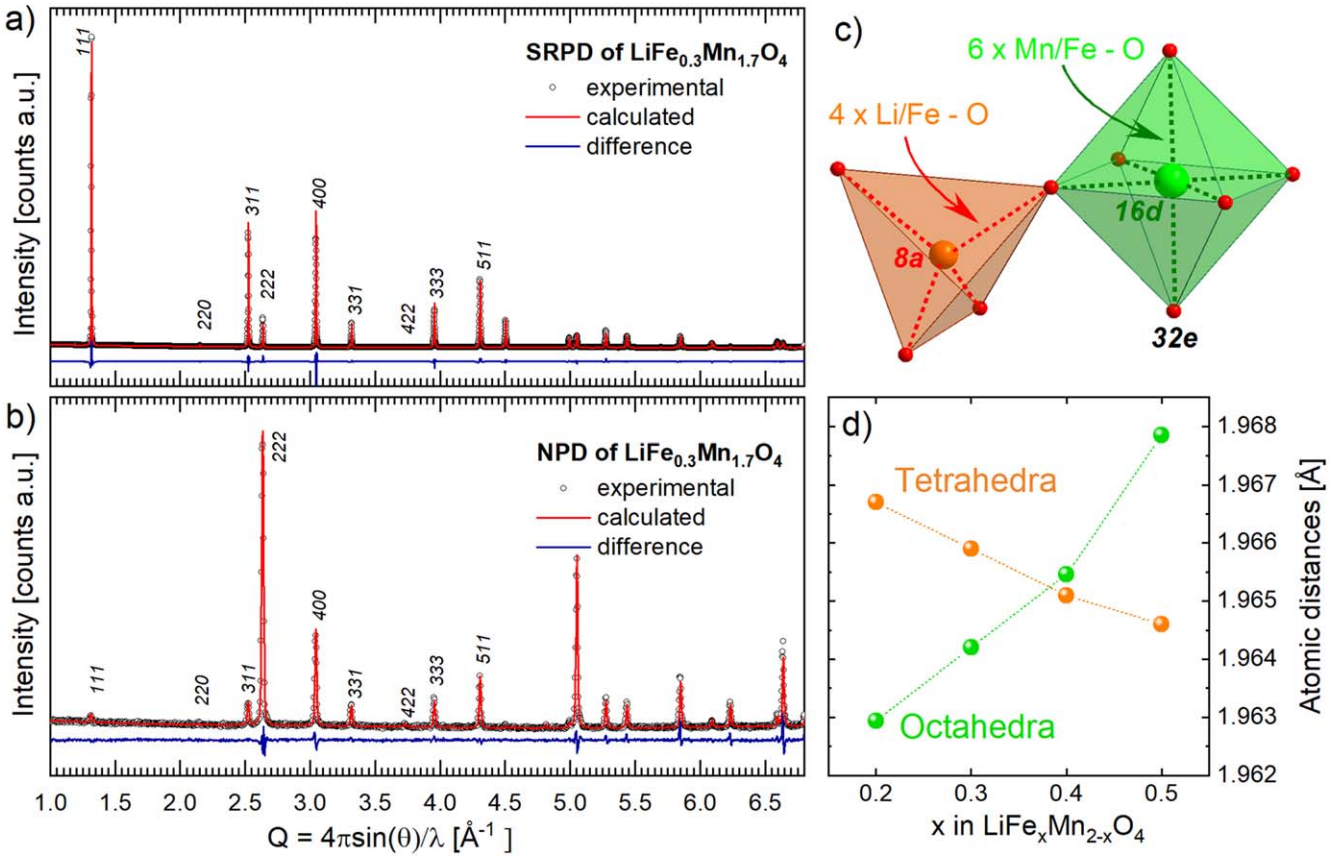

Figure 3. Results of Rietveld analysis from SRPD and NPD data: Experimental (I_{obs}), calculated (I_{calc}) and difference (I_{obs}—I_{calc}) for x = 0.3 exemplarily for SRPD in (a) and for NPD in b); (c) changes of atomic distances in the tetrahedral and octahedral cation coordination polyhedra as a function of x.

Table II. ^{57}Fe Mössbauer hyperfine parameters determined from the analysis of room temperature spectra of $LiFe_xMn_{2-x}O_4$ spinel type materials with $0.2 \leqslant x \leqslant 0.5$ (see Fig. 4). [a] δ isomer shift, [b] Δ quadrupole splitting, 2ε quadrupole shift [c] B_{hf} hyperfine magnetic field, [d] Γ signal linewidth.

x in $LiFe_xMn_{2-x}O_4$	Component	δ [mm.s^{-1}][a]	Δ or 2ε [mm.s^{-1}][b]	B_{hf} [T][c]	Γ [mm.s^{-1}][d]	Relative area [%]	Assignment
0.2	doublet (1)	0.350(1)	0.742(2)	—	0.26(1)	95(2)	Fe^{3+} [*Oh*]
	doublet (2)	0.20(2)	0.27(2)	—	0.27(2)	5(2)	Fe^{3+} [*Td*]
0.3	doublet (1)	0.350(1)	0.744(2)	—	0.26(1)	95(2)	Fe^{3+} [*Oh*]
	doublet (2)	0.21(2)	0.29(2)	—	0.28(2)	5(2)	Fe^{3+} [*Td*]
0.4	doublet (1)	0.349(1)	0.739(2)	—	0.28(1)	95(2)	Fe^{3+} [*Oh*]
	doublet (2)	0.22(2)	0.27(2)	—	0.28(2)	5(2)	Fe^{3+} [*Td*]
0.5	doublet (1)	0.348(1)	0.735(2)	—	0.28(1)	89(2)	Fe^{3+} [*Oh*]
	doublet (2)	0.22(2)	0.29(2)	—	0.27(2)	5(2)	Fe^{3+} [*Td*]
	sextet (1)	0.29(2)	0.01(1)	49(1)	0.45(-)	6(2)	Fe_3O_4 or
	sextet (2)	0.65(5)	0.02(2)	46(1)	0.45(-)		$Li_xFe_{3-x}O_4$

oxidation state and coordination. The spectra recorded with a low-velocity scale ($-3 \leqslant v \leqslant +3$ mm s^{-1}) are presented in Fig. 4. The spectra show a characteristic asymmetric doubled that consist of two components: (1) a major quadrupole doublet and (2) a minor quadrupole doublet, in consistence with the Mössbauer data reported in literature for $LiFe_xMn_{2-x}O_4$ with $x \leqslant 0.5$.[13,16,17,19–22] Hence, all the spectra were tentatively reconstructed considering two components, which led to an excellent fit of the experimental data (χ^2 value close to 1). The refined Mössbauer hyperfine parameters of the main signal (1) are given in Table II (δ = 0.35 mm s^{-1} and Δ = 0.74 mm s^{-1}); they are characteristic of six-fold coordinated high-spin Fe^{3+} ions (on 16*d* octahedral site), in perfect agreement to the literature data.[13,16,17,19–22]

The minor component (2) (relative area: 5%) is characterized by an isomer shift of about 0.20 mm s^{-1} and a smaller quadrupole splitting value (about 0.30 mm s^{-1}). The correct assignment of this component in the Mössbauer spectra collected for $LiFe_xMn_{2-x}O_4$ is center of debates in literature;[13,17,19–22] (i) Talik et al. and Shigemura et al. found an isomer shift of the minor component at 0.354 mm s^{-1} and 0.23 mm s^{-1} respectively, that they both assigned to Fe^{3+} in an octahedral site but with different symmetries[20,21] possibly induced by oxygen defects[21]; (ii) Later, Shigemura et al. and Li et al. assigned the minor component with an isomer shift ranging between 0.21 mm s^{-1} and 0.31 mm s^{-1} to Fe^{3+} in tetrahedral coordination[16,19,22] and further supported their result by NPD[19]; and (iii) Tsuji et al. and Gracia et al. assigned an isomer shift smaller than 0.22 mm s^{-1} to Fe^{4+} or mixed $Fe^{3.5+}$ in octahedral coordination.[13,17] The isomer shift associated to the minor component observed in our study (0.2 mm s^{-1}) is most close those previously attributed in literature to (ii) Fe^{3+} in tetrahedral coordination and (iii) Fe^{4+} in octahedral coordination. The presence of

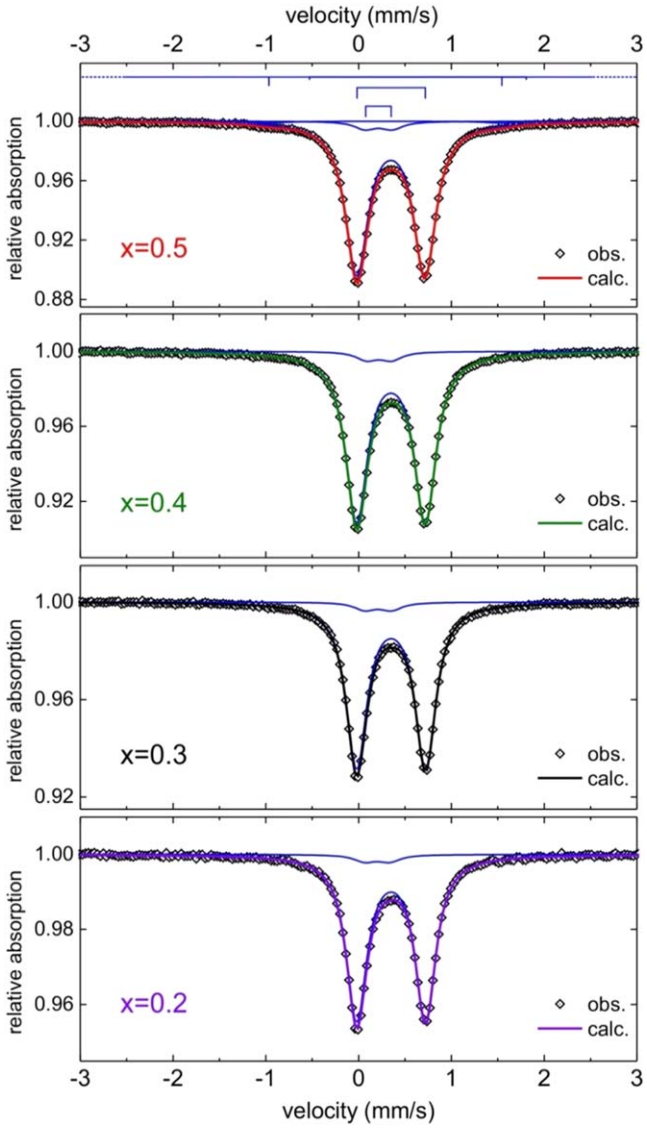

Figure 4. Room temperature ^{57}Fe Mössbauer spectra of the series of $LiFe_xMn_{2-x}O_4$ spinel materials ($0.2 \leqslant x \leqslant 0.5$). The refined hyperfine parameters of the different sub-spectra (highlighted by the blue lines) are gathered in Table II.

Fe in the tetrahedral coordination was proven by Rietveld analysis before, despite in small fractions (less than 4%). The presence of Fe^{4+} cannot be excluded from the Mössbauer data, as its signal would be strongly overlaid by the signal of existing Fe^{3+} in tetrahedral coordination.

Additionally, Mössbauer spectra of the $LiFe_xMn_{2-x}O_4$ compounds were recorded at room temperature with a high-velocity scale ($-12 \leqslant v \leqslant +12$ mm s^{-1}) (Figure S4). An additional minor component, characterized by two sextets, was evidenced for the composition $x = 0.5$. Considering their hyperfine parameters at room temperature (Table II), these magnetically-ordered components may be associated with Fe_3O_4 or $Li_xFe_{3-x}O_4$ spinel, as secondary phase(s), which agrees to the detection of $LiFe_5O_8$ spinel by SRPD and NPD and points out the low stability of the $LiFe_xMn_{2-x}O_4$ spinel by encountering the Fe solubility limitation in between x = 0.4 to 0.5 already.

The CVs of $LiFe_xMn_{2-x}O_4$ with x = 0.2, 0.3, 0.4 and 0.5 reveal three oxidation and three corresponding reduction reactions (Fig. 5). The two peaks in the voltage range between 3.75 to 4.25 V vs Li/Li^+ are characteristic for the $Mn^{4+/3+}$ redox couple, with an order-disorder phase transition upon removing Li^+ from the spinel lattice.[52,53] The high voltage peaks between 4.75 and 5.2 V vs

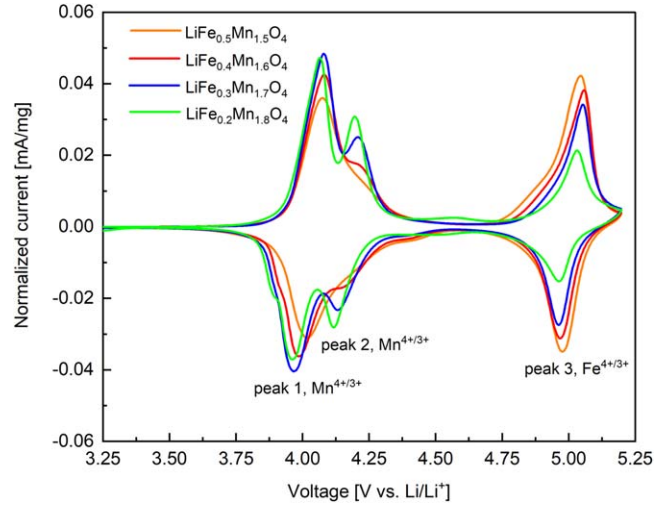

Figure 5. CVs for $LiFe_xMn_{2-x}O_4$ recorded at a scanning rate of 0.028 mV s^{-1} in the range between 3.5 and 5.2 V vs Li/Li^+ for $LiFe_{0.2}Mn_{1.8}O_4$, $LiFe_{0.3}Mn_{1.7}O_4$, $LiFe_{0.4}Mn_{1.6}O_4$ and $LiFe_{0.5}Mn_{1.5}O_4$. Currents are normalized to the mass of active materials in the positive electrode.

Li/Li^+ correspond to the $Fe^{4+/3+}$ redox couple.[19] With increasing Fe content in $LiFe_xMn_{2-x}O_4$, the integrated normalized current intensities attributed to the $Mn^{4+/3+}$ voltage range decrease and those attributed to the $Fe^{4+/3+}$ voltage range increase. This confirms the substitution of Fe^{3+} for Mn^{3+} in $LiFe_xMn_{2-x}O_4$, where 0.2 Mn^{3+} is substituted by 0.2 Fe^{3+} for x = 0.2, 0.3 Mn^{3+} is substituted by 0.3 Fe^{3+} for x = 0.3, 0.4 Mn^{3+} is substituted by 0.4 Fe^{3+} for x = 0.4, and 0.5 Mn^{3+} is substituted by 0.5 Fe^{3+} for x = 0.5, respectively.

Up to x = 0.4, the normalized current peak intensities of the $Mn^{4+/3+}$ redox couple at lower voltages (peak 1, Fig. 5) remain almost unchanged, whereas the normalized current peak intensities for the $Mn^{4+/3+}$ redox couple at higher voltages (peak 2) are subject to significant decrease. It is known that the "valley" between the two $Mn^{4+/3+}$ peaks is reached at electrochemical delithiation states of y = 0.5 in $Li_{1-y}Mn_2O_4$ spinel. At this point, the remaining Li^+ ions start to order in their own *fcc* sublattice.[52,53] This very characteristic order-disorder phase transitions in the 4 V region has been observed for Fe substituted $LiMn_2O_4$ as well.[18] Consistently, our data show the maintenance of the order-disorder phase transition for Fe substitution levels up to x = 0.4. Peak 1 is unaltered; all samples allow the delithiation up to y = 0.5 at the potential of the first $Mn^{4+/3+}$ reaction. The contribution of peak 2 gets lower as the Mn content decreases, and the extraction for y > 0.5 is shifted towards the potential of the $Fe^{4+/3+}$ redox couple.

For a stoichiometric $LiFe_{0.5}Mn_{1.5}O_4$ ($Li^+Fe_{0.5}{}^{3+}Mn_{0.5}{}^{3+}Mn^{4+}O_4$) with only 0.5 mol Mn^{3+} per formula unit, only one $Mn^{4+/3+}$ redox peak should be observed, as the first peak of the $Mn^{4+/3+}$ reaction is expected for delithiation states y < 0.5 in $Li_{1-y}Fe_{0.5}Mn_{1.5}O_4$. The second $Mn^{4+/3+}$ redox peak (peak 2) should disappear completely. However, a small shoulder is still visible at the high voltage side of the first $Mn^{4+/3+}$ redox peak for the $LiFe_{0.5}Mn_{1.5}O_4$ sample. The appearance of this shoulder can have two reasons. The first reason would be an alteration of phase transition characteristics that could be induced by small fractions of Li occupying the 16*d* site. Indeed, the presence of Li on the 16*d* site would frustrate the ordering in the *fcc* sublattice and smears out the sharp double peak characteristics in CV.[52] However, our NPD results falsify this hypothesis, since Li was not detected on the 16*d* site. The other possible reason for the appearance of the shoulder at peak 1 would be a higher fraction of Mn^{3+} than expected for the stoichiometric compound $LiFe_{0.5}Mn_{1.5}O_4$. The possibility of Mn^{3+} overstoichiometry because of oxygen vacancies ($Li^+Fe^{3+}{}_{0.5}Mn^{3+}{}_{0.5+2\delta}Mn^{4+}{}_{1-2\delta}O_{4-\delta}$) was suggested already in the structural section above. The small shoulder at the high voltage side of the first $Mn^{4+/3+}$ redox peak for the $LiFe_{0.5}Mn_{1.5}O_4$ sample

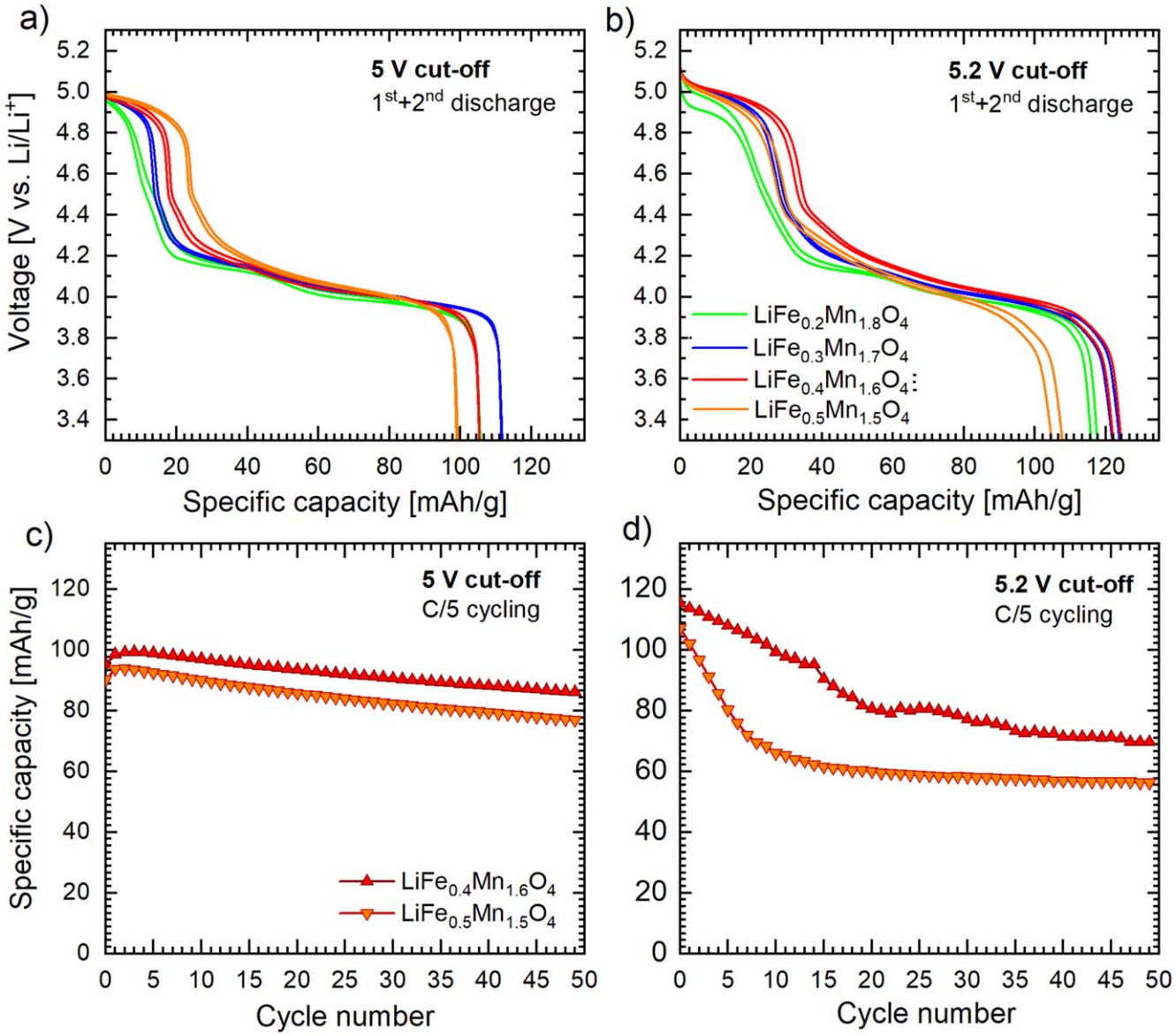

Figure 6. Discharge curves for $LiFe_xMn_{2-x}O_4$ (x = 0.2 to 0.5) at a C/20 rate with two different charging cut-off voltages: (a) 5.0 V and (b) 5.2 V vs Li/Li^+. Specific discharge capacities of $LiFe_xMn_{2-x}O_4$ for x = 0.4 and x = 0.5 cycled at C/5 rate with two different upper charging cut-off voltages: (c) 5.0 V and (d) 5.2 V vs Li/Li^+. The lower cut-off discharging voltage is 3.0 V vs Li/Li^+ for all the samples.

qualitatively matches with the expected level of oxygen defects (<2%)[54–56] and the expected induced Mn^{3+} overstoichiometry. CV has been proven to be a sensitive method for recognizing the presence of Mn^{3+} for different high voltage spinels[56–58] and is here again shown to be a helpful tool to gain insight into the crystal chemistry of the studied spinels. Hence, Mn^{3+} overstoichiometry and oxygen understoichiometry are strongly suggested by two of our results (CV and Rietveld).

The charge-discharge behavior at a C/20 rate at two different upper cut-off voltages (5.0 and 5.2 V vs Li/Li^+) is shown in Figs. 6a and 6b. The discharge curves show "plateaus" at 5.0 V vs Li/Li^+ and in the range between 4.2 and 4.0 V vs Li/Li^+ with a broad transition region in between. The widths of these "plateaus" evolve with the Fe content. In the voltage range between 4.0 and 4.2 vs Li/Li^+ two distinct "plateaus" can be identified for $LiFe_{0.2}Mn_{1.8}O_4$ and $LiFe_{0.3}Mn_{1.7}O_4$, whereas in the same potential range a smoother evolution of the voltage is observed for $LiFe_{0.4}Mn_{1.6}O_4$ and $LiFe_{0.5}Mn_{1.5}O_4$. When charging to a cut-off voltage of 5.0 V vs Li/Li^+, initial specific capacities of 100–110 mAh g^{-1} are obtained (Fig. 6a). The discharge curves with a 5.2 V vs Li/Li^+ upper charging cut-off voltage deliver higher capacities than the one with a charging cut-off at 5.0 V vs Li/Li^+, (Fig. 6b). The samples provide specific capacities of 120–125 mAh g^{-1}, which means an increase by ~20% when rising the upper charging cut-off voltage by 0.2 V from 5.0 V to 5.2 V vs Li/Li^+.

Along with the increase of the higher charging cut-off voltage from 5.0 to 5.2 V vs Li/Li^+, the capacities in the high voltage range (> 4.6 V vs Li/Li^+) undergo significant changes. In the first cycle for the charging cut-off voltage at 5 V vs Li/Li^+, specific capacities of 11, 15, 18 and 24 mAh g^{-1} are obtained for $LiFe_xMn_{2-x}O_4$ with x = 0.2, 0.3, 0.4 and 0.5, respectively. Whereas for the charging cut-off voltage at 5.2 V vs Li/Li^+, specific capacities of 24, 30, 35 and 30 mAh g^{-1} are obtained for $LiFe_xMn_{2-x}O_4$ with x = 0.2, 0.3, 0.4 and 0.5, respectively. This corresponds to 75%, 63%, 57% and 38% of the theoretical capacities associated to the redox couple $Fe^{4+/3+}$ for $LiFe_{0.2}Mn_{1.8}O_4$, $LiFe_{0.3}Mn_{1.7}O_4$, $LiFe_{0.4}Mn_{1.6}O_4$ and $LiFe_{0.5}Mn_{1.5}O_4$, respectively. The CV results already expressed that cycling to 5 V vs Li/Li^+ will not be sufficient to exploit the full $Fe^{4+/3+}$ capacity.

However, even for the higher charging cut-off voltage at 5.2 vs Li/Li^+, the full $Fe^{4+/3+}$ capacity is not yet fully exploit, especially for the samples with higher Fe contents.

The obtained specific discharge capacities agree to the experimental specific discharge capacities reported previously. Indeed, Kawai et al. reported a discharge specific capacity of 125 mAh g^{-1} for $LiFe_{0.5}Mn_{1.5}O_4$, with a high voltage capacity (> 4.5 V vs Li/Li^+) of ∼ 40 mAh g^{-1} after charging to 5.3 V vs Li/Li^+.[9] For an upper charging cut-off voltage of 5.2 V vs Li/Li^+, Ohzuku et al. reported a specific discharge capacity of 110 mAh g^{-1} during the first cycle.[28] For $LiFe_xMn_{2-x}O_4$ with x = 0.1, 0.3 and 0.5, specific discharge capacities of 130, 115 and 120 mAh g^{-1} with high voltage capacities (> 4.5 V vs Li/Li^+) of approximately 10, 20 and 40 mAh g^{-1}, respectively, were reported when charging the battery to 5.3 V vs Li/Li^+ at a C/10 rate.[25] All these studies have in common that the obtained capacities are relatively low compared to the theoretical ones, which is explained by the incomplete $Fe^{4+/3+}$ redox reaction despite very high voltage charging cut-off conditions. The chosen cut-off conditions are always compromises between the extra capacity that can be gained and the side reactions coming from liquid electrolyte decomposition at high voltage that should be mitigated, especially upon long term cycling—as it will be discussed later.

The specific discharge capacities observed upon cycling tests of $LiFe_xMn_{2-x}O_4$ materials at C/5 rate with upper charging cut-off voltages of 5.0 and 5.2 V vs Li/Li^+ are compared in Figs. 6c and 6d for x = 0.4 and 0.5. Along with the charging cut-off voltage of 5.0 V vs Li/Li^+, both materials show capacity fading of ∼ 20% over 50 cycles. In contrast, when operating the cells with a higher charging cut-off voltage of 5.2 V vs Li/Li^+, pronounced decrease of the capacity is observed, which is 39% and 48% for $LiFe_{0.4}Mn_{1.6}O_4$ and $LiFe_{0.5}Mn_{1.5}O_4$ respectively. These results appear in good agreement with the reported cycling stabilities for sol-gel derived $LiFe_{0.5}Mn_{1.5}O_4$ cycled up to 5.3 V vs Li/Li^+ at a cycling rate of C/2 for 70 cycles.[25,33] E.g. Bhaskar et al. reported the capacity retention for $LiFe_{0.5}Mn_{1.5}O_4$ was 66% after 50 cycles and 58% after 70 cycles for the spinel annealed at 600 °C and 72% and 59% after 50 and 70 cycles, respectively, for the spinel post-annealed at 1000 °C.[25] When cycling the post-annealed $LiFe_{0.5}Mn_{1.5}O_4$ for 50 cycles at C/8 to 5.5 V, 68% of the capacity are lost.[33] A similar trend was also observed for $LiFe_{0.5}Mn_{1.5}O_4$ prepared by different synthesis routes, e.g., by solvothermal synthesis, impregnation and template methods with subsequent annealing at 700 °C.[29] These materials show relatively good stability when cycled to 5.0 V vs Li/Li^+, however, with specific capacities below 70 mAh g^{-1}.[29] Increasing the upper charging cut-off voltage for the material prepared from the template method to 5.3 V vs Li/Li^+ results in an initial specific capacity of 103 mAh g^{-1}, but 27% of the capacity are lost already after 16 cycles.[29] Lower charging cut-off voltages of 5.0 V vs Li/Li^+ result in good cycling stability at moderate capacities, whereas charging to voltages higher than 5.0 V vs Li/Li^+ provide enhanced initial specific capacities, but also result in substantial capacity fading.

Capacity fading of electrodes can have several reasons: (i) structural changes in the active material; ii) microstructural degradation of the electrode (micro cracks and loss of contacts); iii) dissolution of soluble elements from the electrode into the electrolyte;[59] (vi) surface orientation of crystalline particles, i.e. crystal habitus;[60] and (v) cathode-electrolyte interface (CEI) formation.[59] For high voltage electrodes, strong capacity degradation is also generally agreed to be an effect of the instability of the conventional electrolytes, when the operational voltage exceeds the oxidation stability limitation.[3] It induces electrolyte decomposition and subsequent deposition of resulting organic and inorganic degradation products on the electrode surface, which adds up to the CEI formation[3,36] and can also cause surface structural changes of the electrode structure.[61] All of these effects would primarily come with capacity fade, due to loss of Li-ions or loss of active material and/or the increase in internal cell resistances, i.e. polarization. In fact, we observe strong correlations between cell degradation

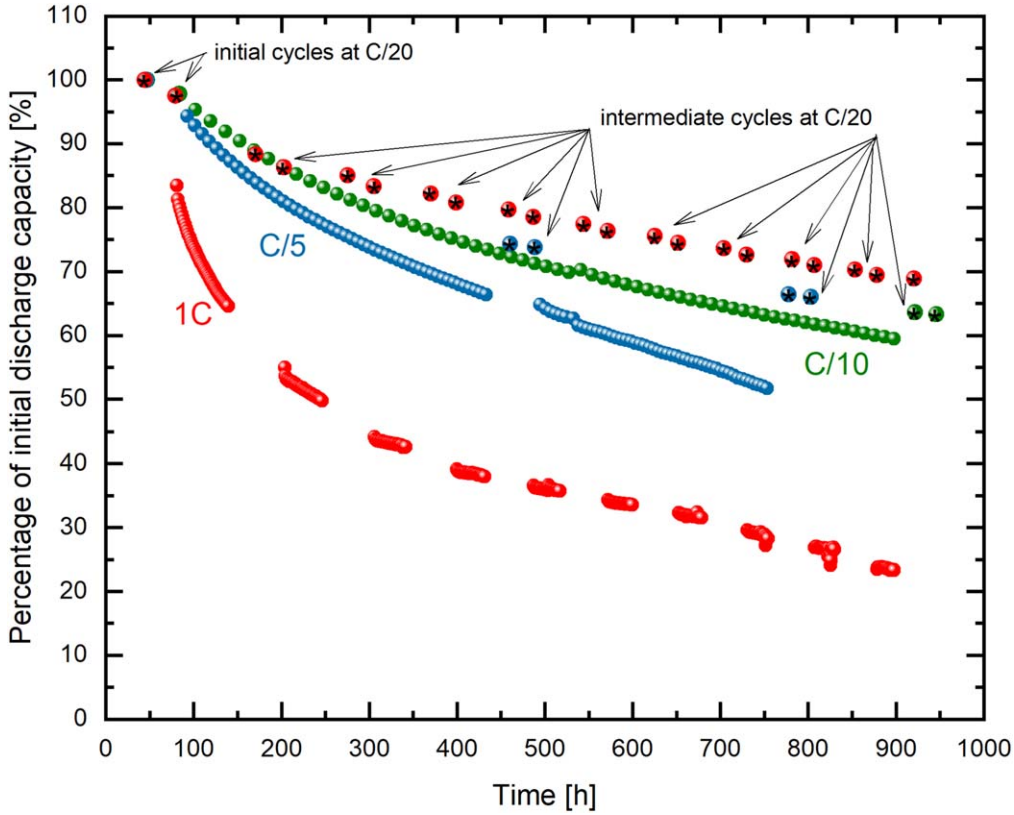

Figure 7. $LiFe_{0.5}Mn_{1.5}O_4$ long term cycling performance over ∼ 900 h in between 3.0 V and 5.2 V vs Li/Li + at different C-rates: 1 C, C/5 and C/10 with intermediate C/20 cycles after 50 cycles each.

and cell polarization. The increasing cell polarization hinders the exploitation of the $Fe^{4+}/^{3+}$ redox capacity (Figures S5 and S6) at thus in itself already causes capacity fading. From the given data, it is difficult to specifically assign a certain mechanism to the observed degradation of the cells. However, we can deduce correlations between capacity degradation and the upper charging cut-off voltage (5.2 V vs Li/Li^+) as well as Fe-content. As such, capacity degradation is more severe for higher cut-off voltages and for higher Fe-content.

To investigate further the degradation mechanism observed upon discharge for $LiFe_{0.5}Mn_{1.5}O_4$ for a upper charging cut-off voltage at 5.2 V vs Li/Li^+, we carried out experiments with different C-rates (C/10, C/5 and 1 C), while allowing intermediate cycles at a much lower current density (C/20) (Fig. 7). The degradation over the whole experimental time increases with the applied C-rate, with 35% degradation for the C/10, 45% for C/5 and 72% for the 1 C cycling. Independent of the C-rate, however, the intermediate cycles at C/20 display a similar strikingly low capacity fading ($\sim$ 30% for all three experiments over $\sim$900 h). This result emphasizes the effect of increased cell polarization in combination with a charging cut-off voltage at 5.2 V vs Li/Li^+, which is too low to exploit the whole capacity of the $Fe^{4+/3+}$ redox. This results in a reversibly retained capacity. The capacity is mostly restored once the current density is lowered and diffusion limitations due to rising overpotentials are overcome.

Accordingly, our data show cell degradation due to two effects: reversible and irreversible degradation. If we consider the capacity fading between the initial cycle at C/20 and the capacity of the intermediate cycle at C/20 after 300 h as a measure of the amount of irreversible degradation only, the irreversible and reversible capacities in our experiments can be treated separately. In view of that, we can conclude that the irreversible capacity due to cell degradation is lower than 20% after 150 cycles at 1 C. For comparison, the well-known $LiNi_{0.5}Mn_{1.5}O_4$ high voltage spinel, operating at 4.7 V vs Li/Li^+, typically shows capacity degradation of $\sim$10% after $\sim$150 cycles.[62,63] With optimized electrolytes, in the near future, and proper materials engineering, these performances might be realized for $LiFe_{0.5}Mn_{1.5}O_4$, while providing similar theoretical capacities and average potentials (in average 4.6 V vs Li/Li^+ and 145 mAh g^{-1}) compared to $LiNi_{0.5}Mn_{1.5}O_4$ (in average 4.7 V vs Li/Li^+ and 145 mAh g^{-1}), but utilizing the more environmentally friendly and more abundant Fe-ion.

Conclusions

$LiFe_xMn_{2-x}O_4$, with $x \leqslant 0.5$, crystallizes in *Fd-3m* spinel structure with partial inversion due to Li^+ and high spin Fe^{3+} mixing on the tetrahedral site as $[Li_{0.98}Fe_{0.02}]^{8a}[Fe_{0.2}Mn_{1.8}]^{16d}O^{32e}{}_4$ for x = 0.2, $[Li_{0.98}Fe_{0.02}]^{8a}[Fe_{0.3}Mn_{1.7}]^{16d}O^{32e}{}_4$ for x = 0.3, $[Li_{0.97}Fe_{0.03}]^{8a}[Fe_{0.4}Mn_{1.6}]^{16d}O^{32e}{}_4$ for x = 0.4, and $[Li_{0.96}Fe_{0.04}]^{8a}[Fe_{0.49}Mn_{1.51}]^{16d}O^{32e}{}_4$ for x = 0.5, respectively. The presence of secondary $LiFe_5O_8$ and Li_2MnO_3 phases as impurities indicate the solubility limit of Fe in between x = 0.4 to 0.5 on the one hand and emphasize the thermodynamic instability—at the given synthesis conditions—on the other hand, as Li_2MnO_3 segregation indicates oxygen deficiencies in the coexisting spinel. Our results suggest that Fe diminishes the stability of the oxygen spinel lattice, leading to oxygen non-stoichiometry and overstoichiometry of Mn^{3+}, which explains the increase in lattice parameter with increasing Fe content for $x \leqslant 0.5$. The $Fe^{4+/3+}$ capacity for the studied samples (x = 0.2 to 0.5) is difficult to exploit fully due to the limitations of the electrolyte stability window. Higher cut-off voltages are associated with higher cell-polarization, which causes severe capacity degradation. Part of this capacity is retained when the current density is lowered, as the increased overpotentials cause a steady decrease of the accessible $Fe^{4+}/^{3+}$ capacity at the given charging cut-off voltage. The fraction of the irreversible capacity fade is still moderate, however, which is a promising starting point for further materials engineering and applicable Fe based high voltage spinels hopefully with compatible electrolytes in the future.

Acknowledgments

The authors would like to thank Alain Wattiaux (ICMCB) for helpful discussion and support. Funding from the German Federal Ministry of Education and Research (BMBF-project DESIREE, grant number 03SF0477A and 03SF0477B), from Region Nouvelle Aquitaine, from the French National Research Agency (STORE-EX Labex Project ANR-10-LABX-76-01) and from ILL for the funding of TR PhD thesis, is acknowledged. Provision of beam time on BL04-MSPD beamline at ALBA was granted through In House proposal 2017042199.

ORCID

Anna Windmüller https://orcid.org/0000-0003-2829-3362
Hans Kungl https://orcid.org/0000-0003-3142-3906
Svitlana Taranenko https://orcid.org/0000-0003-3047-252X
Emmanuelle Suard https://orcid.org/0000-0001-5966-5929
François Fauth https://orcid.org/0000-0001-9465-3106
Mathieu Duttine https://orcid.org/0000-0002-6120-8716
Chih-Long Tsai https://orcid.org/0000-0001-8103-3514
Yasin Emre Durmus https://orcid.org/0000-0001-9245-3549
Hermann Tempel https://orcid.org/0000-0002-9794-6403
Christian Masquelier https://orcid.org/0000-0001-7289-1015
Rüdiger-A. Eichel https://orcid.org/0000-0002-0013-6325
Laurence Croguennec https://orcid.org/0000-0002-3018-0992
Helmut Ehrenberg https://orcid.org/0000-0002-5134-7130

References

1. L. Li, K. S. Lee, and L. Lu, *Funct. Mater. Lett.*, **07**, 1430002 (2014).
2. A. Kraytsberg and Y. Ein-Eli, *Adv. Energy Mater.*, **2**, 922 (2012).
3. W. Li, B. Song, and A. Manthiram, *Chem. Soc. Rev.*, **46**, 3006 (2017).
4. J. Ma, P. Hu, G. Cui, and L. Chen, *Chem. Mater.*, **28**, 3578 (2016).
5. J. Bhattacharya and C. Wolverton, *J. Electrochem. Soc.*, **161**, A1440 (2014).
6. C. M. Julien and A. Mauger, *Ionics*, **19**, 951 (2013).
7. A. Bhaskar, D. Mikhailova, N. Kiziltas-Yavuz, K. Nikolowski, S. Oswald, N. N. Bramnik, and H. Ehrenberg, *Prog. Solid State Chem.*, **42**, 128 (2014).
8. A. Eftekhari, *J. Power Sources*, **124**, 182 (2003).
9. H. Kawai, M. Nagata, M. Tabuchi, H. Tukamoto, and A. R. West, *Chem. Mater.*, **10**, 3266 (1998).
10. J. Molenda, J. Marzec, K. Swierczek, W. Ojczyk, M. Ziemnicki, B. Molenda, M. Drozdek, and R. Dziembaj,, *Solid State Ionics*, **171**, 215 (2004).
11. K. E. Sickafus, J. M. Wills, and N. W. Grimes, *J. Am. Ceram. Soc.*, **82**, 3279 (1999).
12. R. G. Burns, *Mineralogical Applications of Crystal Field Theory* (Cambridge University Press, Cambridge) (1993).
13. M. Gracia, J. R. Gancedo, J. L. Gautier, J. de La Figuera, and J. F. Marco, *Hyperfine Interact.*, **240**, 2327 (2019).
14. Y. G. Mateyshina, U. Lafont, N. F. Uvarov, and E. M. Kelder, *Solid State Ionics*, **179**, 192 (2008).
15. Y. G. Mateyshina, N. F. Uvarov, A. S. Ulihin, and T. Pavlyukhin Yu., *Solid State Ionics*, **177**, 2769 (2006).
16. T. Ohzuku, K. Ariyoshi, S. Takeda, and Y. Sakai, *Electrochim. Acta*, **46**, 2327 (2001).
17. T. Tsuji, M. Nagao, Y. Yamamura, and N. G. Tai,, *Solid State Ionics*, **154-155**, 381 (2002).
18. M. Song, S. U. Ahn, S. G. Kang, and S. H. Chang, *Solid State Ionics*, **111**, 237 (1998).
19. H. Shigemura, M. Tabuchi, H. Kobayashi, H. Sakaebe, A. Hirano, and H. Kageyama, *J. Mater. Chem.*, **12**, 1882 (2002).
20. E. Talik, L. Lipińska, A. Guzik, P. Zajdel, M. Michalska, M. Szubka, M. Kądziołka-Gaweł, and R. L. Paul, *Materials Science-Poland*, **35**, 159 (2017).
21. H. Shigemura, H. Sakaebe, H. Kageyama, H. Kobayashi, A. R. West, R. Kanno, S. Morimoto, S. Nasu, and M. Tabuchi, *J. Electrochem. Soc.*, **148**, A730 (2001).
22. Y. Li et al., *Physica B*, **405**, 4733 (2010).
23. R. D. Shannon, *Acta Cryst A*, **32**, 751 (1976).
24. K. Amine, H. Tukamoto, H. Yasuda, and Y. Fujita, *J. Power Sources*, **68**, 604 (1997).
25. A. Bhaskar, N. N. Bramnik, A. Senyshyn, H. Fuess, and H. Ehrenberg, *J. Electrochem. Soc.*, **157**, A689 (2010).
26. M. Ghiyasiyan-Arani and M. Salavati-Niasari, *Ind. Eng. Chem. Res.*, **58**, 23057 (2019).
27. Y. G. Mateyshina, U. Lafont, N. F. Uvarov, and E. M. Kelder, *Russ. J. Electrochem.*, **45**, 602 (2009).
28. T. Ohzuku, S. Takeda, and M. Iwanaga, *J. Power Sources*, **81-82**, 90 (1999).
29. M. P. Pico, I. Álvarez-Serrano, M. L. López, and M. L. Veiga, *Dalton transactions (Cambridge, England: 2003)*, **43**, 14787 (2014).
30. E. Talik, L. Lipińska, P. Zajdel, A. Załóg, M. Michalska, and A. Guzik, *J. Solid State Chem.*, **206**, 257 (2013).

31. H. Liu, R. Tian, Y. Jiang, X. Tan, J. Chen, L. Zhang, Y. Guo, H. Wang, L. Sun, and W. Chu, *Electrochim. Acta*, **180**, 138 (2015).
32. I. Taniguchi and Z. Bakenov, *Powder Technol.*, **159**, 55 (2005).
33. A. Bhaskar, N. N. Bramnik, D. M. Trots, H. Fuess, and H. Ehrenberg, *J. Power Sources*, **217**, 464 (2012).
34. S. Kuppan, H. Duncan, and G. Chen, *Physical chemistry chemical physics: PCCP*, **17**, 26471 (2015).
35. W. Xu, X. Chen, F. Ding, J. Xiao, D. Wang, A. Pan, J. Zheng, X. S. Li, A. B. Padmaperuma, and J.-G. Zhang, *J. Power Sources*, **213**, 304 (2012).
36. Q. Li, Y. Wang, X. Wang, X. Sun, J.-N. Zhang, X. Yu, and H. Li, *ACS Appl. Mater. Interfaces*, **12**, 2319 (2020).
37. J. B. Goodenough and Y. Kim, *Chem. Mater.*, **22**, 587 (2010).
38. Y.-R. Zhu and T.-F. Yi, *Ionics*, **22**, 1759 (2016).
39. N.-S. Choi, J.-G. Han, S.-Y. Ha, I. Park, and C.-K. Back, *RSC Adv.*, **5**, 2732 (2015).
40. R. Sun, P. Jakes, S. Eurich, D. van Holt, S. Yang, M. Homberger, U. Simon, H. Kungl, and R.-A. Eichel, *Appl. Magn. Reson.*, **49**, 415 (2018).
41. F. Fauth, I. Peral, C. Popescu, and M. Knapp, *Powder Diffr.*, **28**, S360 (2013).
42. E. Suard and A. Hewat, *Neutron News*, **12**, 30 (2001).
43. H. M. Rietveld, *J. Appl. Crystallogr.*, **2**, 65 (1969).
44. B. H. Toby and R. B. von Dreele, *J. Appl. Crystallogr*, **46**, 544 (2013).
45. A. Boulineau, L. Croguennec, C. Delmas, and F. Weill, *Chem. Mater.*, **21**, 4216 (2009).
46. A. Boulineau, L. Croguennec, C. Delmas, and F. Weill, *Solid State Ionics,*, **180**, 1652 (2010).
47. D. M. Cupid, T. Lehmann, T. Bergfeldt, H. Berndt, and H. J. Seifert, *J. Mater. Sci.*, **48**, 3395 (2013).
48. J. Bréger, M. Jiang, N. Dupré, Y. S. Meng, Y. Shao-Horn, G. Ceder, and C. P. Grey, *J. Solid State Chem.*, **178**, 2575 (2005).
49. L. A. Picciotto and M. M. Thackeray,, *Mater. Res. Bull.*, **21**, 583 (1986).
50. D. M. Cupid, A. Reif, and H. J. Seifert, *Thermochim. Acta*, **599**, 35 (2015).
51. C. Luo and M. Martin, *J. Mater. Sci.*, **42**, 1955 (2007).
52. Y. Gao, J. Reimers, and J. Dahn, *Phys. Rev. B*, **54**, 3878 (1996).
53. M. Bianchini, F. Fauth, E. Suard, J.-B. Leriche, C. Masquelier, and L. Croguennec, *Acta Cryst.*, **B71**, 688 (2015).
54. N. Reeves-McLaren, J. Sharp, H. Beltrán-Mir, W. M. Rainforth, and A. R. West, *Proc. R. Soc.*, **472**, 20140991 (2016).
55. P. Strobel, F. Le Cras, L. Seguin, M. Anne, and J. M. Tarascon, *J. Solid State Chem.*, **135**, 132 (1998).
56. A. Windmüller, C. Bridges, C.-L. Tsai, S. Lobe, C. Dellen, G. Veith, M. Finsterbusch, S. Uhlenbruck, and O. Guillon, *ACS Appl. Energy Mater.*, **1**, 715 (2018).
57. R. Alcántara, M. Jaraba, P. Lavela, J. L. Tirado, P. Biensan, A. de Guibert, C. Jordy, and J. P. Peres, *Chem. Mater.*, **15**, 2376 (2003).
58. N. Kuwata, S. Kudo, Y. Matsuda, and J. Kawamura, *Solid State Ion.*, **262**, 165 (2014).
59. M. M. Kabir and D. E. Demirocak, *Int. J. Energy Res.*, **41**, 1963 (2017).
60. J. S. Kim, K. S. Kim, W. Cho, W. H. Shin, R. Kanno, and J. W. Choi, *Nano Lett.*, **12**, 6358 (2012).
61. X. Fan and C. Wang, *Chem. Soc. Rev.*, **50**, 10486 (2021).
62. G. Liang, V. K. Peterson, K. W. See, Z. Guo, and W. K. Pang, *J. Mater. Chem. A*, **8**, 15373 (2020).
63. X. Yu, W. A. Yu, and A. Manthiram, *Small methods*, **5**, 2001196 (2021).